UC Irvine
UC Irvine Previously Published Works

Title

Lightweight Head-Mounted Optical Coherence Tomography Scope for Longitudinal, Intact-Skull Imaging of Ischemic Stroke in Freely Behaving Mouse

Permalink

https://escholarship.org/uc/item/8t69v3hc

Journal

ACS Photonics, 13(9)

ISSN

2330-4022

Authors

Wang, Jingyi
Malone, Hayden
Wei, Shuang
et al.

Publication Date

2026-05-06

DOI

10.1021/acsphotonics.6c00287

Copyright Information

This work is made available under the terms of a Creative Commons Attribution License, available at https://creativecommons.org/licenses/by/4.0/

Peer reviewed

eScholarship.org Powered by the California Digital Library
University of California

ACS Photonics

Open Access

This article is licensed under CC-BY-NC-ND 4.0

pubs.acs.org/journal/apchd5

Article

Lightweight Head-Mounted Optical Coherence Tomography Scope for Longitudinal, Intact-Skull Imaging of Ischemic Stroke in Freely Behaving Mouse

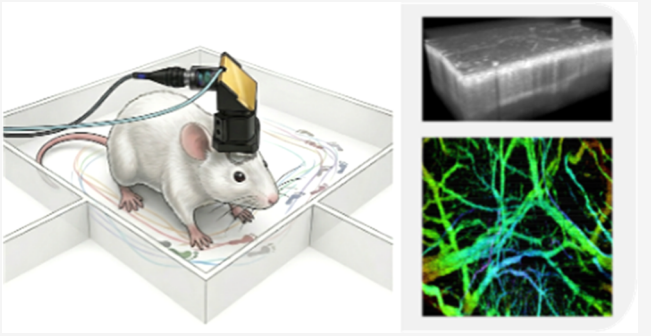
Jingyi Wang, Hayden Malone, Shuang Wei, Khoa Huynh, Lidek Chou, Ron D. Frostig, and Zhongping Chen*

Cite This: *ACS Photonics* 2026, 13, 2678−2686

Read Online

ACCESS | Metrics & More | Article Recommendations

ABSTRACT: Understanding the dynamic progression of an ischemic stroke under physiologically relevant conditions is essential for advancing therapeutic strategies. Here, we present a miniaturized, lightweight (1.5 g), head-mounted Doppler optical coherence tomography system capable of high-resolution, high-speed imaging through the intact skull in freely behaving mice. The system enables real-time monitoring of cerebral vasculature and structural dynamics without the need for invasive cranial window implantation. Using a permanent middle cerebral artery occlusion (pMCAo) model, we conducted longitudinal imaging of stroke progression across multiple time points: baseline, immediately post-surgery within 3 h, and at days 1 and 2 post-pMCAo. Volumetric angiography (OCTA) allowed depth-resolved vascular mapping, and comparative analysis of anesthetized versus freely moving conditions revealed activity-dependent changes in microvascular flow. Moreover, K-means-based segmentation was applied to quantify blood vessel density (BVD) across nine cortical regions of interest for a more accurate and robust analysis compared with that of the traditional method. BVD declined post-pMCAo and showed region-specific recovery trends, with some areas demonstrating reperfusion and new vessel formation by day 2. Structural OCT also revealed cortical shrinkage following a stroke, with partial recovery observed over time. This study represents the first demonstration of OCT imaging in freely moving ischemic stroke models and provides new insights into vascular and structural responses under natural behavior. Our findings underscore the utility of head-mounted OCT systems for studying cerebrovascular diseases in a minimally invasive, longitudinal, and behaviorally relevant context—laying the foundation for future stroke research and therapeutic evaluation.



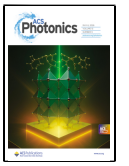
KEYWORDS: *optical coherence angiography, freely moving imaging, miniature OCT, cerebral vasculature, brain imaging, neurovascular*

INTRODUCTION

Stroke is the fifth leading cause of death, responsible for about 1 in every 20 deaths in the United States in 2022. Ischemic stroke, which accounts for 87% of all strokes, occurs when a blood vessel supplying the brain is obstructed and contributes to approximately 3.59 million deaths globally.[1] In addition to its high mortality, stroke is a major cause of severe long-term disability, particularly affecting mobility in over half of stroke survivors aged 65 and older.[2] Ischemic stroke patients who receive emergency treatment of clot-dissolving medicine within the first 4 h or the new thrombectomy technique, with better success, can increase the chance of recovery. The goal of therapy in acute ischemic strokes is to preserve tissue in areas with reduced perfusion to prevent infarction. Tissue in this oligemic zone can be preserved by restoring blood flow and enhancing collateral circulation. However, the benefits of reperfusion are time-dependent, as prompt intervention is crucial to minimize the effects of ischemia.[3] Despite ongoing research, no neuroprotective agents have demonstrated a clear benefit in improving clinical outcomes. Therefore, studying vascular dynamics is critical for gaining a more comprehensive understanding of stroke progression and advancing treatment options.

A significant consequence of ischemic stroke is the reduction of cerebral blood flow, which impairs brain function. The

Received: February 1, 2026
Revised: April 8, 2026
Accepted: April 9, 2026
Published: April 17, 2026



ACS Publications

© 2026 The Authors. Published by American Chemical Society

https://doi.org/10.1021/acsphotonics.6c00287
ACS Photonics 2026, 13, 2678−2686

Downloaded from pubs.acs.org/apchd5/article-pdf/13/9/2678/6621917/3/acsphotonics.6c00287.pdf by UNIV OF CALIFORNIA IRVINE user on 06 November 2026

middle cerebral artery (MCA), the most commonly affected artery in stroke that supplies the lateral cerebral cortex, is responsible for motor and sensory functions of the face and upper extremities.[3] Previous studies using the ischemic stroke rat model achieved by pMCAo have demonstrated that sensory stimulation of the whisker can protect the cortex from ischemic stroke.[4−8] However, traditional imaging methods require the animal to be anesthetized or immobilized, which limits the effectiveness of the data obtained. One of the reasons is the effect of the anesthesia, which includes the blood flow reduction and decreased global cerebral metabolism.[9] Moreover, the absence of the animal's self-determined activity distorts the interpretation of brain responses, as the natural behavior and environmental interactions are not captured. To address this challenge, there is increasing interest in head-mounted microscope devices for various imaging modalities. Each imaging modality offers unique advantages with certain trade-offs.[10,11] For example, photoacoustic microscopy (PAM) extends deep into the tissue and offers insights into functional and molecular information but generally offers lower spatial resolution and lacks the ability to directly visualize fine structural details at the cellular or tissue layer level. Compared with fluorescence imaging that lacks depth information, multiphoton microscopy (MPM) offers cellular-level resolution but has a restricted field of view (FOV) in the range of hundreds of micrometers to a millimeter and slow imaging speeds. Optical coherence tomography (OCT), on the other hand, strikes a balance by offering adequate penetration depth and a large FOV without sacrificing high resolution of the micrometer level, making it increasingly applied in brain imaging. A basic OCT system provides high-resolution cross-sectional imaging and readily enables the reconstruction of three-dimensional (3D) tissue structural images. More importantly, functional extensions of OCT—such as OCT angiography (OCTA) and Doppler OCT (DOCT)—significantly broaden its capabilities, allowing for detailed imaging of blood vessels and comprehensive analysis of vascular networks.[12−17]

We previously reported the development of a miniaturized, lightweight, head-mounted OCT scope designed for imaging in freely moving mice.[18] This device has demonstrated high reliability and stability in acquiring OCT and OCTA images from brain regions of interest (ROI), such as the hippocampus and visual cortex—areas commonly implicated in neurodegenerative diseases like Alzheimer's disease. The scope features a focal-adjustable design, enabling compatibility with various brain imaging procedures at different depths. In earlier studies, imaging was performed through a cylindrical cannula sealed with a glass coverslip over the targeted brain region. While the transparent glass ensured high laser transmission and minimized light scattering, the surgical implantation process required firm fixation and inevitably caused slight tissue compression due to applied pressure. Moreover, cranial window implantation surgery can induce both acute and chronic physiological changes in the brain.[19] Cortical inflammation resulting from skull removal or thinning has been shown to alter neural activity.[20] In particular, for regions such as the barrel cortex—commonly studied in ischemic stroke models—evoked hemodynamic and neural responses have been reported to be suppressed for up to 2 weeks following cranial window implantation.[21] These alterations can significantly affect the accuracy of disease mechanism analysis during the early postsurgical period. Therefore, it is crucial to explore brain imaging approaches that allow for data acquisition through the intact skull, minimizing physiological disruptions and preserving native brain function.

In this study, we employed a miniaturized head-mount OCT scope that weighs only 1.5 g to monitor the progression of ischemic stroke induced by pMCAo through the intact skull in freely behaving mouse. The system used a high-speed swept-source laser centered at 1310 nm, providing a scanning speed of 200 kHz and a high axial resolution of 7.4 μm. The scope offers a large FOV of 4 × 4 mm, enabling wide-area cerebral imaging. We compared vascular images acquired from both immobilized and freely moving mice and observed activity-related changes in cerebral blood flow. Building upon these findings, we conducted continuous imaging for 3 h immediately following pMCAo surgery, followed by additional imaging sessions at 1 and 2 days post-surgery to track longitudinal vascular changes. Early postischemic vascular dynamics are of particular interest because rapid therapeutic intervention after stroke is strongly associated with improved outcome. Compared with imaging paradigms that require chronic cranial window implantation and recovery before longitudinal observation, the lightweight head-mounted OCT system used here allows imaging to begin within minutes after pMCAo, enabling direct monitoring of acute cerebrovascular changes in freely moving mice. To the best of our knowledge, this represents the first demonstration of an OCT imaging in freely moving animals following ischemic stroke induction. The approach offers a unique opportunity to investigate stroke progression under physiologically relevant conditions and holds promise for advancing our understanding of stroke pathology. Ultimately, this technique may contribute to the development of more effective therapeutic strategies aimed at preventing life-threatening complications, limiting widespread brain damage and reducing long-term disability.

METHODS

Imaging Device and System Setup

The platform used in this study was built upon our previously reported head-mounted OCT system and further refined for the present study, including improved system sensitivity (104 dB) and a modified baseplate design to accommodate the pMCAo surgical preparation. The fiber-based OCT system, as shown in Figure 1a, utilizes a swept source laser scanning at 200 kHz and centered at 1310 nm (SL132121, Thorlabs Inc.). The laser output is no less than 20 mW and split into the sample arm and reference arm by the 90:10 fiber coupler. Two fiber circulators are used to direct the laser and isolate the back-reflected from the incident beam in the reference and

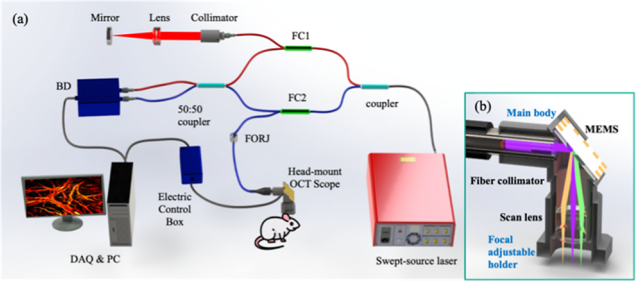


Figure 1. System Design. (a) Schematic of the imaging system. BD: balance detector; FC: fiber circulator; FORJ: fiber optical rotary joint; (b) enlarged view of the head-mounted OCT probe and its optical layout.

https://doi.org/10.1021/acsphotonics.6c00287
ACS Photonics 2026, 13, 2678−2686

Downloaded from pubs.acs.org/apchd5/article-pdf/13/9/2678/6621917/3/acsphotonics.6c00287.pdf by UNIV OF CALIFORNIA IRVINE user on 06 November 2026

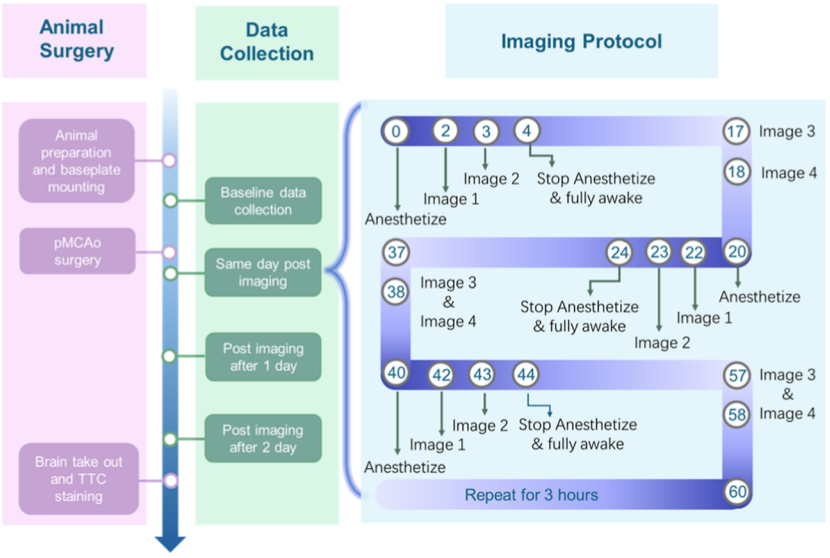


Figure 2. Experimental protocol illustrating the animal preparation and imaging timeline. The colored gradient along the imaging protocol timeline indicates the awake state of the mouse—lighter shades represent higher levels of wakefulness. This schematic outlines the experiment workflow.

sample arm, separately. In the reference arm, the light is collimated and reflected back through an optical path to maximize the coupling efficiency at the end of the 50:50 coupler. In the sample arm, the laser exits the circulator and is collimated by a GRIN-lens collimator (50-1310A-APC, Thorlabs Inc.), which is integrated into the custom-designed head-mounted OCT scope. A key component enabling miniaturization of the OCT scope is dual-axis microelectromechanical systems (MEMS) for beam scanning. The customized bare dual-axis MEMS mirror (A7M20.2, Mirrorcle Tech) integrated with a 2 mm diameter aluminum-coated surface provides an optical scanning range of approximately ±22 degrees per axis. With a resonant frequency of 1.3 kHz, the MEMS enables fast scanning. It is driven via a surface-soldered flexible printed circuit that is connected to the electric control box by miniature insulated wires, ensuring high flexibility for freely moving. In this system, the drive signal is optimized to generate 2000 A-lines per frame, achieving a frame rate of 100 Hz. The focused beam is delivered to the sample through a 5 mm diameter, 10 mm focal length achromatic doublet lens with C-coating (AC-050-010-C, Thorlabs Inc.). The backscattered signal from the sample is returned to the 50:50 coupler, where it interferes with the reference signal. This interferometric signal is then detected by a balanced photodetector and recorded by the data acquisition system (ATS9371, AlazarTech).

The structure and optical path of the head-mounted scope are illustrated in Figure 1b. The collimated beam, scanned by a MEMS mirror, is focused by a lens mounted in a focal-adjustable holder, producing a 4 × 4 mm scanning area. The lightweight design of the head-mounted scope allows the mouse to acclimate immediately without additional training or external support components. During data acquisition, the mouse behaves naturally within its cage. A 1 m fiber optic cable connects to the scope, offering sufficient mobility, while a fiber optic rotary joint (FORJ) is incorporated to minimize torque induced by fiber twisting during movement. This compact and flexible setup enables reliable OCT imaging and real-time brain monitoring in freely moving mice.

Animal Preparation

All experiments were managed according to the National Institutes of Health guidelines for animal care and use and were authorized by the University of California, Irvine Institutional Animal Care and Use Committee (IACUC).

Presurgical Preparation. The male C57BL mice, 27−32 g (Jackson Laboratories, Sacramento, CA, USA), were housed individually in enriched cages placed in a temperature, humidity, and light-controlled room (12 hour cycle: 6 am-6 pm). Mice were handled daily for 20 min for 3−5 days until the day of the experiment. Mice were anesthetized with 4% isoflurane for induction and then maintained at 1.5% through the duration of the procedure. Body temperature was maintained at 37 °C via a self-regulating thermal blanket (Homeothermic heating blanket, Harvard Apparatus). The surgical site was disinfected with 10% povidone-iodine (PVP prep pads, Medline) and 70% isopropyl alcohol wipes, then local anesthesia (2% lidocaine) was applied subcutaneously to the midline of the head. One milliliter of 5% warmed dextrose (subcutaneous) and atropine (0.05 mg/kg, bodyweight [bw], intramuscular) was administered for hydration and control secretions, respectively.

Surgical Preparation. Two cranial regions were prepared: an intact-skull imaging window for OCT/OCTA acquisition and a separate surgical window for pMCAo induction located anterior and lateral to the imaging window. The imaging window remained unthinned to preserve the native skull integrity. The pMCAo surgical window was created outside the imaging field, allowing the same cortical region to be imaged longitudinally before and after artery occlusion. During surgery, the detachable head-mounted OCT scope was removed, while the baseplate remained fixed to the skull for subsequent repositioning during imaging sessions. Using a sterile technique, a midline incision was made from bregma to lambda. Underlying soft tissue was resected approximately 2 mm dorsal to the sagittal suture and extended to ∼10 mm ventral to accommodate the baseplate for the scope fixture. Though the imaging window position was limited by the area of the pMCAo surgical window, using the Mouse Brain Atlas,[22] the baseplate was positioned to potentially capture a portion of the dorsal barrel cortex. The skull surface was thoroughly cleaned and dried to promote the proper adhesion of the material to the bone. Cyanoacrylate glue (Professional liquid super glue, Loctite) was added to the base of the implant and affixed to the skull. Three sides were fortified with dental cement (Cold Cure Dental Cement, TEETS) to secure the implant in place, leaving the ipsilateral MCA region (to the imaging area) exposed for subsequent pMCAo surgery. A thin layer of glue was added to the imaging window to maintain the transparency and prevent tissue regrowth. The skull of the imaging window was kept intact and not thinned. The pMCAo surgical window that was positioned anterior and lateral to the implant 1.5 mm × 1.5 mm was made by thinning and removing the skull. 2% agarose was placed over the surgical window, and then the area was sealed with liquid silicone (Silicone mold rubber, Smooth-On) to protect the cortex during baseline Doppler imaging.

Permanent Middle Cerebral Artery Occlusion (pMCAo). Following baseline imaging and pre-pMCAo, the silicone and agarose were removed. A 30G needle was carefully used to excise the dura mater from the surgical window, and the M1 segment of the MCA

Downloaded from pubs.acs.org/apchd5/article-pdf/13/9/2678/6621917/3/acsphotonics.6c00287.pdf by UNIV OF CALIFORNIA IRVINE user on 06 November 2026

https://doi.org/10.1021/acsphotonics.6c00287
ACS Photonics 2026, 13, 2678−2686

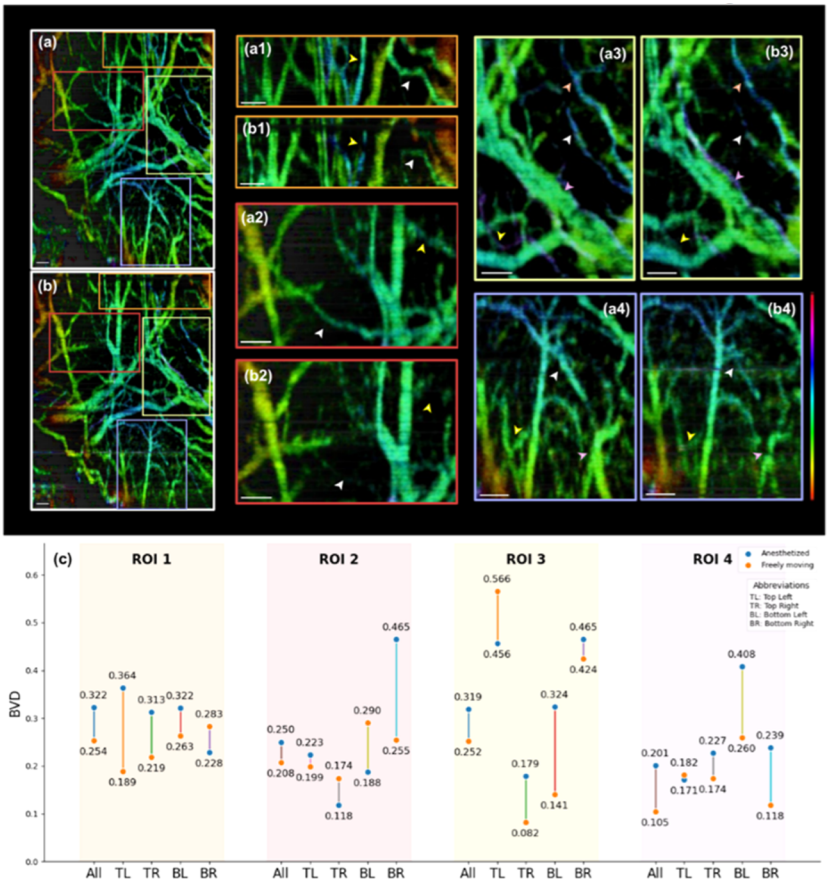


Figure 3. Comparison of cortical vasculature between anesthetized and freely moving states. (a,b) show the OCTA images of cortical blood vessels acquired under anesthetized and freely moving conditions, respectively. (a1−a4) and (b1−b4) show enlarged views of the corresponding ROIs from the anesthetized and freely moving states, respectively. (c) ROI-based BVD comparison for the selected regions shown in (a,b). For each ROI, BVD was quantified for the whole ROI and its 2 × 2 subregions (TL, TR, BL, and BR) using K-means-based segmentation.

was identified. A small, threaded needle was inserted and passed under the artery. The thread was then cut and tied to form a double ligature, effectively occluding blood flow as previously described.[23]

Postsurgical Preparation. Analgesics (flunixin and buprenorphine) and an antibiotic (Enrosite) were administered subcutaneously following both implant and pMCAo surgeries: flunixin meglumine (2 mg/kg), buprenorphine (0.05 mg/kg), and enrofloxacin (5 mg/kg), respectively. The mouse was allowed to recover in a clean cage before imaging sessions.

Histology. To confirm ischemic conditions were achieved and determine the location of the infarct, 2 mm coronal brain sections were stained with 2,3,5-triphenyltetrazolium chloride (2% TTC) for 30 min in the dark.[24] TTC is a redox indicator; active mitochondria stain red, which indicates healthy tissue, while infarcted regions appear white due to metabolic inactivity. Sections were photographed with a digital camera.

Data Collection

The experimental procedure is illustrated in Figure 2. The process begins with animal preparation and the implantation of a custom-designed baseplate. This baseplate was modified to leave sufficient space for subsequent surgical procedures. Following baseplate mounting, animals were given a 1 day recovery period before baseline imaging was performed. The pMCAo surgery was then conducted to induce ischemic stroke.

To capture hyperacute ischemic events during the critical early phase following pMCAo, OCT/OCTA imaging was performed continuously for 3 h post-surgery. Given the importance of this period, the imaging timeline was carefully structured with sessions at 20 min intervals, allowing for high temporal resolution of stroke progression. At each imaging cycle, brief anesthetized scans were first acquired to provide motion-reduced reference images at a defined post-pMCAo time point. After recovery from isoflurane, additional data sets were acquired while the mouse was freely moving. This design enabled within-session comparison between anesthetized and awake vascular signals. The primary longitudinal analysis in this study focused on the freely moving condition, as the main purpose of the head-mounted imaging platform was to capture poststroke vascular dynamics during natural behavior. The anesthetized scans were therefore used mainly as reference and comparison measurements rather than as an independent longitudinal imaging arm.

Each imaging session included two physiological states: anesthetized and freely moving. At the beginning of each session (minute 0), anesthesia (isoflurane) was applied, and two 1 min OCT/OCTA scans were recorded. At minute 4, anesthesia was discontinued, and the mouse was returned to its home cage. The mouse was awake and started moving within a few minutes. To make sure the mouse is fully awake and naturally behaving, enough time is given before imaging data collection. At minutes 17 and 18, two imaging data sets are recorded when the mouse is freely moving in the cage. During the final minute of the interval (minute 19), preparations were made for the next session, and anesthesia was reapplied to restart the cycle.

This imaging cycle—comprising both anesthetized and awake conditions—was repeated three times per hour, resulting in a total of nine imaging sessions during the initial 3 h postoperative window. Additional OCT/OCTA imaging was conducted on postoperative day 1 and day 2 to monitor longitudinal changes in vascular structure and function.

The color gradient along the imaging timeline in Figure 2 represents the mouse's level of wakefulness, with lighter shades indicating a more awake state. This design allows visualization of both

Downloaded from pubs.acs.org/apchd5/article-pdf/13/9/2678/6621917/3/acsphotonics.6c00287.pdf by UNIV OF CALIFORNIA IRVINE user on 06 November 2026

https://doi.org/10.1021/acsphotonics.6c00287
ACS Photonics 2026, 13, 2678−2686

the temporal structure of data acquisition and the physiological state under which each data set was collected.

RESULTS

We acquired and analyzed both the OCT and OCTA images for each imaging data set. A comparison was performed between vascular images obtained under anesthetized conditions and those acquired during free movement to assess activity-related changes in cerebral blood flow. Additionally, longitudinal monitoring of ischemic stroke progression, revealed by a three-dimensional OCT image and a vasculature map, was conducted. To quantify vascular changes over time, blood vessel density (BVD) was calculated and used as a key metric for evaluating alterations in the cortical microvasculature following pMCAo.

OCT/OCTA Imaging Processing

Each OCT image frame, comprised of 2000 A-lines and 1000 B-scan positions, is collected for a three-dimensional tissue structural image. OCTA requires multiple images at the same position to reveal the signal difference. In this study, a subsequent 6x B-scan is acquired at each position to extract the vasculature image.

To address potential phase instability caused by the motion of freely moving mice, we employed the intensity-based Doppler variance method to reconstruct angiographic images.[25] The technique, originally derived from Doppler variance using the autocorrelation of the OCT signal, was further modified by incorporating averaging in both the lateral and the axial directions to enhance the signal-to-noise ratio (SNR). The method maps blood vessels based on the amplitude component of the complex OCT signal, making it more robust to motion artifacts. The algorithm is described by the following equation:

$$\delta^2 = \frac{1}{T^2}\left[1 - \frac{\sum_{j=1}^{J}\sum_{n=1}^{N}(|A_{j,n}||A_{j+1,n}|)}{\sum_{j=1}^{J}\sum_{n=1}^{N}\frac{1}{2}(|A_{j,n}|^2 + |A_{j+1,n}|^2)}\right] \quad (1)$$

The reliability and repeatability of awake OCT/OCTA imaging with this head-mounted platform were established in our previous work;[18] the present study extends that validated framework to longitudinal intact-skull imaging of ischemic stroke in freely behaving mice.

State-Dependent Variations in Cerebral Vasculature

OCT data were collected through the unthinned skull over the dorsal barrel cortical region. By collecting and analyzing the OCT complex data, as described above, the Doppler variance was calculated with B-scan cross-section OCT images of each position. These images were then resliced along the z-axis, aligned with the optical path to generate en-face angiography. Volumetric OCTA data were further projected into two-dimensional, depth-encoded images representing a total imaging depth of 450 μm, as shown in Figure 3. In these images, color represents the axial depth of the vascular signal, with superficial vessels shown in blue and deeper vessels shown in red/yellow. The color bar in Figure 3 indicates this depth-dependent encoding. Figure 3a,b shows the angiography acquired using the head-mounted scope in anesthetized and freely moving mice, respectively. While major vessels are consistently visible in both conditions, noticeable differences in microvascular flow patterns were observed. Selected regions were highlighted with colored boxes, and their corresponding magnified views are shown in (a1) and (a3) for the anesthetized state and (b1) and (b3) for the freely moving state. In (a1) and (b1), yellow and white arrows indicate clear differences in small vessel flow. In (a2) and (b2), a branching vessel (white arrow) is visible only under anesthesia as well as another shorter vessel (yellow arrow). In (a3) and (b3), the pink arrow highlights a vessel branch adjacent to a larger vessel that becomes active only during movement. Similarly, the orange-arrow vessel demonstrates greater flow in the moving state, whereas the white-arrow vessel exhibits a higher activity under anesthesia. The yellow-arrowed vessel in the lower left corner appears exclusively in the anesthetized condition. In (a4) and (b4), arrows indicate vessels with distinct differences in flow intensity between states. Additionally, a major vessel in the left-central region exhibits an increased flow when the mouse is moving. Importantly, these findings were consistently observed across five independent imaging sessions under identical conditions, confirming the reproducibility of the observed vascular dynamics. To complement the qualitative comparison in Figure 3a,b, we further quantified BVD in the selected ROIs using K-means-based segmentation. As shown in Figure 3c, the BVD was calculated for each whole ROI as well as its 2 × 2 subregions (TL, TR, BL, and BR). The paired comparisons reveal region-dependent differences between anesthetized and freely moving conditions, consistent with the localized vascular variations observed in the OCTA images. Notably, some subregions showed larger state-dependent differences than the corresponding all-ROI averages, indicating that the vascular variations were spatially localized rather than uniform across the selected regions.

Structural Changes in OCT Cross-Sections after pMCAo

Figure 4 presents the cortical structural changes before and after the ischemic stroke induction. (a) Anatomical reference of the mouse brain, adapted from the Allen Mouse Brain Atlas, highlighting the dorsal barrel cortex region of interest. (b) Three-dimensional cortical structure reconstructed from OCT data acquired prior to pMCAo surgery, using 1000 B-scans with 2000 A-lines per frame. The unthinned, transparent skull enables clear visualization of cortical layers. (b1−b4) show representative cross-sectional B-scan images at different y-axis positions from the baseline data set.

In contrast, (c) presents the 3D structural reconstruction from data acquired 1 day after pMCAo surgery. Corresponding B-scan frames are shown in (c1−c4). Notably, a distinct separation between cortical layers near the skull surface is observed, as indicated by colored arrows and boxes. This structural gap suggests possible tissue shrinkage resulting from an ischemic injury. The shrinkage appears to be progressive and is most pronounced on day 1 post-surgery. Imaging at the same positions on day 2 post-surgery revealed partial recovery, although the separation between layers was still detectable, indicating ongoing but incomplete restoration of cortical structure. Additionally, a slight decrease in skull transparency was observed over time, as indicated by increased signal scattering in the top layer of the cross-sectional OCT images. Nevertheless, the transparency remained sufficient to maintain a relatively high image quality for both the OCT and OCTA throughout the imaging sessions. To quantitatively support the structural alteration observed in the OCT cross-sectional images after pMCAo, we performed a semiautomated analysis of the thin low-scattering band-like feature in the superficial cortex. With the skull−tissue interface as the anatomical

Downloaded from pubs.acs.org/apchd5/article-pdf/13/9/2678/6621917/3/acsphotonics.6c00287.pdf by UNIV OF CALIFORNIA IRVINE user on 06 November 2026

https://doi.org/10.1021/acsphotonics.6c00287
ACS Photonics 2026, 13, 2678−2686

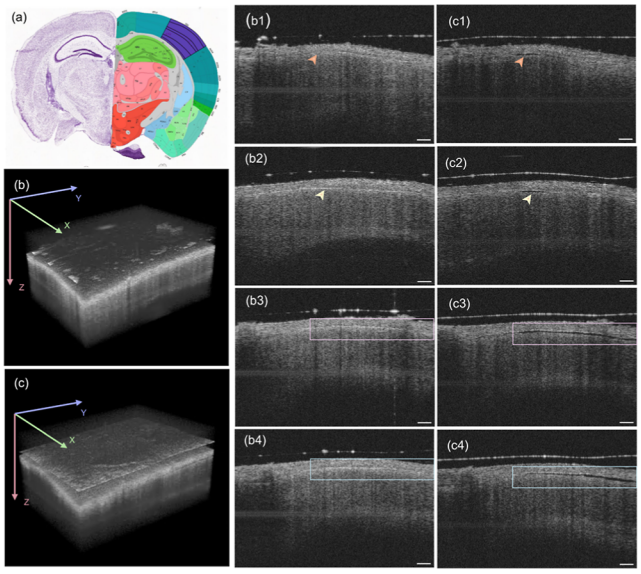


Figure 4. Assessment of cortical structure before and after pMCAo. (a) Anatomical reference of the mouse brain, adapted from the Allen Mouse Brain Atlas. (b,c) show the three-dimensional cortical structure imaged before and 1 day after pMCAo induction, respectively. (b1−b4) present representative cross-sectional B-scan images at different positions along the *y*-axis prior to pMCAo, while (c1−c4) show corresponding cross-sections acquired 1 day post-pMCAo. The color blocks and arrows highlight structural alterations associated with ischemic injury. Scale bar 200 μm.

reference, the feature was identified within a constrained depth range below the skull. In the valid regions, the band on day 1 post-pMCAo was located at an average depth of 407.23 ± 56.25 μm below the skull bottom and had an average thickness of 39.88 ± 7.20 μm across 155 sampling points. By day 2 post-pMCAo, the average thickness decreased to 17.78 μm, indicating a partial reduction of this structural change. This quantitative analysis further supports cross-sectional cortical changes.

Longitudinal Ischemic Stroke Monitoring

In addition to structural OCT images of the cortex, vascular changes are of particular interest due to their relevance to behavioral states. Figure 5 presents longitudinal depth-encoded OCTA images acquired before and after pMCAo. (a) Displays the baseline depth-coded OCTA image of the dorsal cortical region prior to surgery. In this image, the color bar represents the axial depth of the projected vascular signal, with superficial vessels appear in blue, while deeper vasculature is rendered in red, corresponding to a depth of 550 μm. Panels (b)−(j) show sequential OCTA images acquired over a 3 h period immediately after pMCAo, with 20 min intervals between scans, as described in the Methods section. The top of each image is oriented toward the MCA ligation site and infarcted region. Notably, vessels near the center of the field exhibit the most pronounced changes—initially vanishing and then gradually reperfusing over time. Although the overall trend suggests vascular remodeling, the progression is not strictly linear. Panels (k) and (l) show OCTA images acquired at 1 and 2 days post-surgery, respectively, highlighting longer-term vascular recovery. By day 1, most vasculature appears reestablished, and by day 2, increased flow volume and the reappearance of some smaller vessels are evident, suggesting ongoing reperfusion. Panel (m) provides a schematic of the

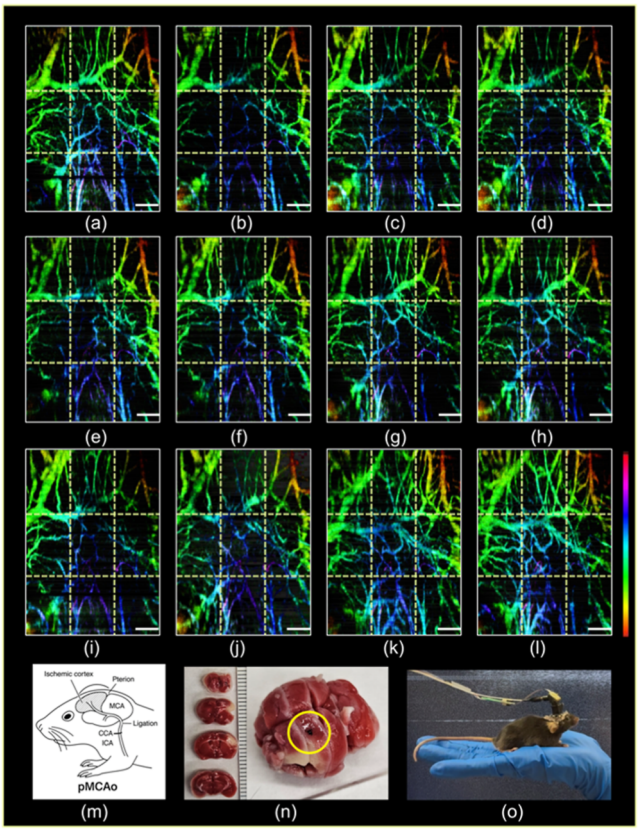


Figure 5. Longitudinal analysis of vasculature alterations using OCTA following pMCAo. (a) Baseline OCTA image of the dorsal cortical region prior to pMCAo induction. The color bar indicates vascular depth, with superficial vessels shown in blue and deeper vessels shown in red. (b−j) show sequential OCTA images acquired within the first 3 h post-surgery at 20 min intervals, capturing the progression of vascular changes over time. (k,l) represent OCTA images obtained at 1 and 2 days post-pMCAo, respectively, providing insight into longer-term vascular remodeling. (m) A schematic illustration of the pMCAo procedure. (n) TTC-stained histological image confirming the infarct region; the marked area indicates the OCT imaging region, and the black ink marks the center of the imaging window. (o) Photograph of the mouse equipped with the head-mounted OCT scope during the imaging session. Mesh lines were overlaid to divide the image into 9 ROIs, arranged in a 3 × 3 grid. Regions 1 to 3 correspond to the top row, regions 4 to 6 to the middle row, and regions 7 to 9 to the bottom row. Scale bar 500 μm.

pMCAo procedure, with labeled anatomical landmarks, while the panel (n) shows TTC-stained histological sections confirming the infarct location, the black ink indicating the center of the imaging window. Finally, panel (o) presents a photograph of the mouse wearing the head-mounted OCT scope, illustrating the system's compact and lightweight design, which permits imaging during natural movement.

Quantitative Analysis of Blood Vessel Density Using K-Means Clustering

BVD was selected as the primary quantitative metric in this study because it provides a robust measure of perfused vascular occupancy for regional and longitudinal comparison while remaining relatively tolerant to signal variability in repeated awake imaging through the intact skull. BVD was quantified from en-face OCTA projection image using an intensity-based K-means clustering approach. For each image, the OCTA image was first converted to grayscale and normalized to the

Downloaded from pubs.acs.org/apchd5/article-pdf/13/9/2678/6621917/3/acsphotonics.6c00287.pdf by UNIV OF CALIFORNIA IRVINE user on 06 November 2026

https://doi.org/10.1021/acsphotonics.6c00287
ACS Photonics 2026, 13, 2678−2686

range [0, 1] to standardize the intensity scale across images while preserving relative contrast. The normalized image was then reshaped into a 1D array of pixel intensities and segmented using K-means clustering with $K = 2$. Each en-face OCTA image was then divided into smaller ROIs using a 3×3 grid, as shown in Figure 5. The labeling is region 1−3 on the first row, 4−6 in the center row, and 7−9 of the bottom row. This segmentation allowed us to perform a localized analysis on each region, helping us identify areas with varying BVD.

K-means clustering, an unsupervised machine learning algorithm was then applied to segment the blood vessels from the surrounding tissues.[26−28] The algorithm partitions the image pixels into K clusters based on pixel intensity, minimizing the variance within each cluster. The Euclidean distance used for clustering is calculated as

$$d(x, \mu_k) = \sqrt{\sum_{i=1}^{n} (x_i - \mu_{k,i})^2} \tag{2}$$

where x_i represents the intensity value of the pixel and $\mu_{k,i}$ is the centroid of cluster k. In this study, $K = 2$ was selected to provide binary separation between the higher-intensity vascular signal and the lower-intensity background signal in the processed OCTA projections. The cluster with the higher mean intensity was assigned as the vessel class, since vascular structures generally appeared brighter than the surrounding background in the en-face OCTA images. BVD was defined as the fraction of pixels assigned to this vessel class within the ROI. The same processing pipeline was applied to all images for consistency.

$$\text{BVD} = \frac{\text{number of blood vessel pixels}}{\text{total number of pixels in the region}} \times 100\%$$

K-means clustering offers several advantages over traditional thresholding methods for blood vessel segmentation in OCTA images. Traditional thresholding requires the use of a fixed intensity threshold to distinguish blood vessels from the surrounding tissues. However, this method can be ineffective in the presence of varying contrast, lighting, or noise across different images. A fixed threshold might result in under-segmentation (missing smaller vessels) or oversegmentation (misclassifying nonvessel areas as vessels).

In contrast, K-means clustering dynamically assigns pixels to clusters based on their intensity values, making it adaptive to the image's inherent intensity distribution. This adaptability allows K-means to segment blood vessels more accurately. For OCTA images, the dynamic approach is a significant advantage, as blood vessels can have varying intensity levels across different regions or time points, and a fixed threshold may not capture these variations effectively. Furthermore, K-means can handle multiple intensity levels, improving segmentation in complex images with varied vascular structures and making it more robust to noise and variations in illumination.

Moreover, K-means clustering is computationally efficient and works well for large data sets, making it particularly suitable for analyzing multiple OCTA images. The unsupervised nature of K-means eliminates the need for manual labeling or threshold selection, which is often impractical in medical imaging, where annotating large data sets is time-consuming and prone to error.

The heatmap, as shown in Figure 6, provides a comprehensive view of the BVD across nine ROIs over a

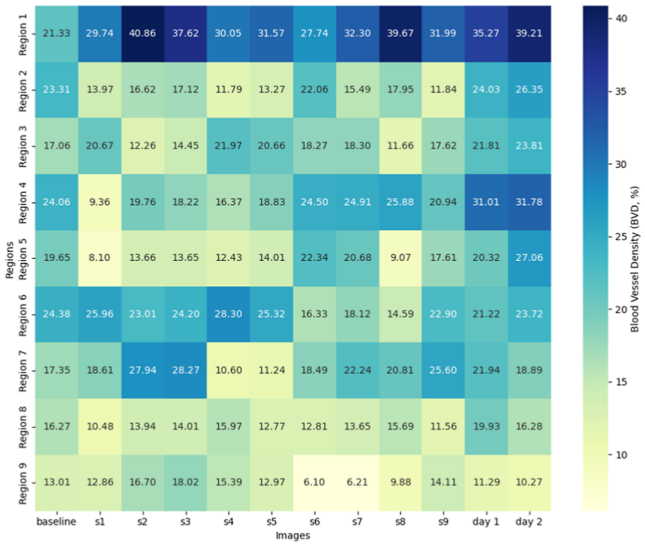


Figure 6. Heatmap visualization of BVD derived from K-means-based segmentation.

series of time points, ranging from baseline to day 2. A closer inspection of the data reveals both spatial and temporal variations in BVD across the image regions and over time. Overall, BVD significantly decreases immediately following pMCAo, followed by gradual recovery, reaching levels comparable to or exceeding baseline by day 1 or 2.

Region 1 consistently shows higher BVD values across all time points and exhibits the most significant vascular presence. Starting at 21.33% at baseline and peaking at 40.86% during the early time points, ending with 39.21% on day 2. This suggests robust reperfusion and neovascularization in the barrel cortex and around the ischemic region. Regions 2−5 show marked BVD reduction immediately after pMCAo, followed by progressive recovery, reaching or exceeding baseline levels by day 1 and stabilizing thereafter. Regions 6 and 7 are relatively stable across the timeline, although fluctuation happens, but they return to the same level as the baseline after 1 day. This suggests that while these regions maintain relatively good vascularity, there might be some degree of remodeling or stabilization by the end of the study period. Notably, Region 7 shows greater variability, potentially reflecting localized vascular adaptation or restructuring. In contrast, Regions 8 and 9 consistently present lower BVD values across all time points. Although a temporary decline is observed, recovery toward the baseline is evident by day 2. For instance, Region 8 drops from 16.27% at baseline to 10.48% post-surgery and recovers to 16.28% by day 2.

These findings highlight regional heterogeneity in the vascular response to ischemic injury and demonstrate the potential of miniaturized OCTA for dynamic and longitudinal vascular monitoring in freely moving animals. The heterogeneous BVD changes across ROIs may reflect spatial differences in the local vascular territory, collateral perfusion, and ischemic severity within the cortical area affected by pMCAo. One possible explanation is the spatial variation in collateral support from adjacent vascular territories, which may contribute to the heterogeneous recovery patterns observed across the ROIs. Regions showing earlier recovery of the vascular signal may

Downloaded from pubs.acs.org/apchd5/article-pdf/13/9/2678/6621917/3/acsphotonics.6c00287.pdf by UNIV OF CALIFORNIA IRVINE user on 06 November 2026

https://doi.org/10.1021/acsphotonics.6c00287
ACS Photonics 2026, 13, 2678−2686

retain better collateral support or less severe vascular impairment, whereas persistently low-BVD regions may correspond to more severely affected areas with limited reperfusion. Pro-angiogenic processes may also contribute to later vascular changes, although this was not directly evaluated in the present study.

DISCUSSION

In this study, we developed a miniaturized head-mounted DOCT system for longitudinal imaging of an ischemic stroke through the intact skull in freely behaving mice. This platform provides a minimally invasive and behaviorally relevant approach for real-time monitoring of cerebrovascular dynamics, offering a powerful tool for investigating the progression and recovery mechanisms of ischemic stroke. To the best of our knowledge, this represents the first demonstration of in vivo OCTA imaging in freely moving mice following ischemic stroke induction. The imaging system is compact and lightweight (1.5 g), integrates a 200 kHz swept-source OCT centered at 1310 nm, and achieves an axial resolution of 7.4 μm with a 4 × 4 mm FOV. The system also features a focal-adjustable design compatible with various imaging depths and surgery protocols and incorporates a fiber-optic rotary joint to prevent torsional strain during movement. Importantly, this design avoids the need for skull thinning or open cranial window implantation, preserving physiological conditions and enabling long-term, repeatable imaging with minimal tissue damage.

Using the pMCAo model, we conducted longitudinal imaging at baseline, during the first 3 h post-surgery (in 20 min intervals), and on days 1 and 2 post-occlusion. Because the anesthetized and awake data sets were acquired sequentially within the same experimental course, the anesthetized data were interpreted primarily as motion-reduced reference measurements for state comparison. Accordingly, the longitudinal progression shown in this study emphasizes the freely moving condition, which represents the central application scenario of the proposed imaging platform. Our data reveal distinct temporal and spatial changes in cortical microvasculature and structure. Comparisons between anesthetized and freely moving states demonstrated clear activity-dependent blood flow differences, suggesting that motion and behavioral state significantly influence vascular dynamics. OCTA was used to generate volumetric depth-resolved vascular maps. BVD was quantified using K-means-based segmentation across nine ROIs, providing detailed insight into poststroke vascular remodeling. Results showed significant decreases in BVD shortly after stroke induction followed by region-specific recovery patterns. Some cortical regions, particularly those near the infarct site, exhibited reperfusion and even new vessel formation by day 2, whereas others remained reduced or changed more gradually, highlighting the heterogeneous vascular response to ischemic injury. Additionally, structural OCT images revealed cortical shrinkage near the skull interface post-pMCAo, with partial recovery observed over time.

This study has its limitations. The sample size remains modest; the observation window mainly covers the acute to early subacute stage after pMCAo, and the quantitative analysis is centered primarily on structural vascular metrics rather than additional functional hemodynamic parameters. Accordingly, the present work should be interpreted as establishing longitudinal intact-skull OCT/OCTA monitoring of early poststroke vascular changes in freely moving mice, rather than as a complete characterization of chronic stroke progression. Although BVD provided a robust quantitative readout for regional and longitudinal comparison in the present awake imaging paradigm, additional hemodynamic parameters such as flow velocity, flow volume, and vessel diameter may further enrich the interpretation of poststroke vascular dynamics. Reliable extraction of these parameters in freely moving animals imaged through the intact skull will require dedicated acquisition and validation and remains an important direction for future work.

Future improvements could include the integration of complementary imaging modalities such as multiphoton microscopy or photoacoustic imaging to achieve cellular-level resolution or oxygen saturation mapping. Enhancing skull transparency by using long-term optical clearing techniques could further improve image quality over extended periods. Finally, applying this platform to study neurodegenerative disease progression or therapeutic efficacy would expand its utility across a broader range of biomedical research applications.

In summary, our work establishes a versatile and scalable imaging tool for neuroscience, paving the way for new discoveries in brain function, vascular pathology, and treatment development under naturalistic conditions.

ASSOCIATED CONTENT

Data Availability Statement

The data are available from the corresponding author upon reasonable request.

AUTHOR INFORMATION

Corresponding Author

Zhongping Chen − *Department of Electrical Engineering and Computer Science, University of California Irvine, Irvine, California 92612, United States; Department of Biomedical Engineering, University of California Irvine, Irvine, California 92697, United States; Beckman Laser Institute, University of California Irvine, Irvine, California 92612, United States;* orcid.org/0000-0002-4584-4560; Email: z2chen@uci.edu

Authors

Jingyi Wang − *Department of Electrical Engineering and Computer Science, University of California Irvine, Irvine, California 92612, United States; Beckman Laser Institute, University of California Irvine, Irvine, California 92612, United States;* orcid.org/0000-0002-8722-2401

Hayden Malone − *Department of Neurobiology and Behavior, University of California Irvine, Irvine, California 92612, United States*

Shuang Wei − *Department of Biomedical Engineering, University of California Irvine, Irvine, California 92697, United States; Beckman Laser Institute, University of California Irvine, Irvine, California 92612, United States*

Khoa Huynh − *Department of Neurobiology and Behavior, University of California Irvine, Irvine, California 92612, United States*

Lidek Chou − *Beckman Laser Institute, University of California Irvine, Irvine, California 92612, United States*

Ron D. Frostig − *Department of Biomedical Engineering, University of California Irvine, Irvine, California 92697,*

Downloaded from pubs.acs.org/apchd5/article-pdf/13/9/2678/6621917/3/acsphotonics.6c00287.pdf by UNIV OF CALIFORNIA IRVINE user on 06 November 2026

https://doi.org/10.1021/acsphotonics.6c00287
ACS Photonics 2026, 13, 2678−2686

United States; Department of Neurobiology and Behavior, University of California Irvine, Irvine, California 92612, United States

Complete contact information is available at: https://pubs.acs.org/10.1021/acsphotonics.6c00287

Author Contributions

J.W. designed and developed the system and experiment, analyzed the data, and wrote the paper with H.M. H.M. and K.H. conducted surgeries and postoperative animal monitoring. S.W. helped with animal control and the imaging procedure. L.C. helped with the prototype. R.F. and Z.C. supervised the project.

Funding

National Institute of Health Grant (R01EB-030558, R01HL-125084,R01EB-030024, R01NS-126526); Air Force Office Scientific Research (FA9550-23-1-0685) from Z.C. National Institutes of Health Grant R01NS126526 from RDF.

Notes

The authors declare no competing financial interest.

REFERENCES

(1) Martin, S. S.; Aday, A. W.; Allen, N. B.; Almarzooq, Z. I.; Anderson, C. A. M.; Arora, P.; Avery, C. L.; Baker-Smith, C. M.; Bansal, N.; Beaton, A. Z.; et al. Heart Disease and Stroke Statistics: A Report of US and Global Data From the American Heart Association. *Circulation* **2025**, *151* (8), e41−e660.

(2) Jackson, G.; Chari, K. National Hospital Care Survey Demonstration Projects: Stroke Inpatient Hospitalizations. *Natl. Health Stat. Rep.* **2019**, 1−11.

(3) Lui, F.; Suheb, M. Z. K.; Patti, L. *Ischemic Stroke*; StatPearls Publishing: Treasure Island (FL), 2025.

(4) Zhu, J.; Hancock, A. M.; Qi, L.; Telkmann, K.; Shahbaba, B.; Chen, Z.; Frostig, R. D. Spatiotemporal dynamics of pial collateral blood flow following permanent middle cerebral artery occlusion in a rat model of sensory-based protection: a Doppler optical coherence tomography study. *Neurophotonics* **2019**, *6* (04), 1.

(5) Qi, L.; Zhu, J.; Hancock, A. M.; Dai, C.; Zhang, X.; Frostig, R. D.; Chen, Z. Fully distributed absolute blood flow velocity measurement for middle cerebral arteries using Doppler optical coherence tomography. *Biomed. Opt. Express* **2016**, *7* (2), 601−615.

(6) Frostig, R. D.; Lay, C. C.; Davis, M. F. A rat's whiskers point the way toward a novel stimulus-dependent, protective stroke therapy. *Neuroscientist* **2013**, *19* (3), 313−328.

(7) Lay, C. C.; Frostig, R. D. Complete protection from impending stroke following permanent middle cerebral artery occlusion in awake, behaving rats. *Eur. J. Neurosci.* **2014**, *40* (9), 3413−3421.

(8) Lay, C. C.; Jacobs, N.; Hancock, A. M.; Zhou, Y.; Frostig, R. D. Early stimulation treatment provides complete sensory-induced protection from ischemic stroke under isoflurane anesthesia. *Eur. J. Neurosci.* **2013**, *38* (3), 2445−2452.

(9) Hudetz, A. G. General anesthesia and human brain connectivity. *Brain Connect.* **2012**, *2* (6), 291−302.

(10) Zhong, X.; Liang, Y.; Wang, X.; Lan, H.; Bai, X.; Jin, L.; Guan, B. O. Free-moving-state microscopic imaging of cerebral oxygenation and hemodynamics with a photoacoustic fiberscope. *Light Sci. Appl.* **2024**, *13* (1), 5.

(11) Guan, H.; Li, D.; Park, H. C.; Li, A.; Yue, Y.; Gau, Y. A.; Li, M. J.; Bergles, D. E.; Lu, H.; Li, X. Author Correction: Deep-learning two-photon fiberscopy for video-rate brain imaging in freely-behaving mice. *Nat. Commun.* **2022**, *13* (1), 5817.

(12) Ren, H.; Ding, Z.; Zhao, Y.; Miao, J.; Nelson, J. S.; Chen, Z. Phase-resolved functional optical coherence tomography: simultaneous imaging of in situ tissue structure, blood flow velocity, standard deviation, birefringence, and Stokes vectors in human skin. *Opt. Lett.* **2002**, *27* (19), 1702−1704.

(13) Chen, Z.; Milner, T. E.; Dave, D.; Nelson, J. S. Optical Doppler tomographic imaging of fluid flow velocity in highly scattering media. *Opt. Lett.* **1997**, *22* (1), 64−66.

(14) Chen, Z.; Milner, T. E.; Srinivas, S.; Wang, X.; Malekafzali, A.; van Gemert, M. J.; Nelson, J. S. Noninvasive imaging of in vivo blood flow velocity using optical Doppler tomography. *Opt. Lett.* **1997**, *22* (14), 1119−1121.

(15) Qiu, S.; Arthur, A.; Jiang, Y.; Miao, Y.; Li, Y.; Wang, J.; Tadir, Y.; Lane, F.; Chen, Z. OCT angiography in the monitoring of vaginal health. *APL Bioeng.* **2023**, *7* (4), 046112.

(16) Song, Y.; Wei, S.; Zou, H.; Wang, J.; Zhang, F.; Zhou, Q.; Jing, Y.; Chen, Z. Enhanced photo-sono therapy with dual-frequency ultrasound. *APL Bioeng.* **2025**, *9* (4), 046109.

(17) Jiang, Y.; Wang, J.; Murthy, R. S.; Patel, P.; Chen, Z. Intracoronary Optical Coherence Tomography: Technological Innovations and Clinical Implications in Cardiology. *Curr. Treat. Options Cardiovasc. Med.* **2025**, *27* (1), 44.

(18) Wang, J.; Ye, Q.; Chou, L.; Qiu, S.; Xu, X.; Chen, Z. Miniaturized Head-Mount Doppler Optical Coherence Tomography Scope for Freely Moving Mouse. *ACS Photonics* **2024**, *11* (8), 3381−3389.

(19) Cramer, S. W.; Carter, R. E.; Aronson, J. D.; Kodandaramaiah, S. B.; Ebner, T. J.; Chen, C. C. Through the looking glass: A review of cranial window technology for optical access to the brain. *J. Neurosci. Methods* **2021**, *354*, 109100.

(20) Plog, B. A.; Lou, N.; Pierre, C. A.; Cove, A.; Kenney, H. M.; Hitomi, E.; Kang, H.; Iliff, J. J.; Zeppenfeld, D. M.; Nedergaard, M.; et al. When the air hits your brain: decreased arterial pulsatility after craniectomy leading to impaired glymphatic flow. *J. Neurosurg.* **2020**, *133* (1), 210−223.

(21) Park, H.; You, N.; Lee, J.; Suh, M. Longitudinal study of hemodynamics and dendritic membrane potential changes in the mouse cortex following a soft cranial window installation. *Neurophotonics* **2019**, *6* (01), 1.

(22) Paxinos, G.; Franklin, K. B. *The Mouse Brain in Stereotaxic Coordinates*; Academic Press, 2019.

(23) Davis, M. F.; Lay, C.; Frostig, R. D. Permanent cerebral vessel occlusion via double ligature and transection. *J. Vis. Exp.* **2013**, 50418.

(24) Bederson, J. B.; Pitts, L. H.; Germano, S. M.; Nishimura, M. C.; Davis, R. L.; Bartkowski, H. M. Evaluation of 2,3,5-triphenyltetrazolium chloride as a stain for detection and quantification of experimental cerebral infarction in rats. *Stroke* **1986**, *17* (6), 1304−1308.

(25) Liu, G.; Chou, L.; Jia, W.; Qi, W.; Choi, B.; Chen, Z. Intensity-based modified Doppler variance algorithm: application to phase instable and phase stable optical coherence tomography systems. *Opt. Express* **2011**, *19* (12), 11429−11440.

(26) Lloyd, S. Least squares quantization in PCM. *IEEE Trans. Inf. Theory* **1982**, *28* (2), 129−137.

(27) MacQueen, J. Some methods for classification and analysis of multivariate observations. In *Proceedings of the Fifth Berkeley Symposium on Mathematical Statistics and Probability*; University of California press, 1967; Vol. *5*, pp 281−298.

(28) Jain, A. K.; Dubes, R. C. *Algorithms for Clustering Data*; Prentice-Hall, Inc., 1988.

Downloaded from pubs.acs.org/apchd5/article-pdf/13/9/2678/6621917/3/acsphotonics.6c00287.pdf by UNIV OF CALIFORNIA IRVINE user on 06 November 2026